

Inferring Cosmic String Tension through the Neural Network Prediction of String Locations in CMB Maps

Razvan Ciuca,^{a,b,c} Oscar F. Hernández^{a,b}

^aDepartment of Physics, McGill University,
3600 rue University, Montréal, QC, H3A 2T8, Canada

^bMarianopolis College,
4873 Westmount Ave., Westmount, QC H3Y 1X9, Canada

^cSchool of Computer Science, McGill University,
3480 rue University, Montréal, QC, H3A 0E9, Canada

E-mail: razvan.ciuca@mail.mcgill.ca, oscarh@physics.mcgill.ca

Abstract. In references [1, 2] we constructed a convolutional neural network used to estimate the location of cosmic strings in simulated Cosmic Microwave Background (CMB) temperature anisotropy maps. We derived a connection between the estimates of cosmic string locations by this neural network and the posterior probability distribution of the cosmic string tension $G\mu$. Here we improve the calculation of the posterior distribution of the string tension $G\mu$. We also improve our previous convolutional neural network by using residual networks. We apply our new neural network and posterior calculation method to maps from the same simulation used in references [1, 2] and quantify the improvement.

Contents

1	Introduction	1
2	A better way to compute the posterior probability	3
2.1	The posterior probability in terms of the evidence provided by the neural network	3
2.2	Conditions on the neural network f	3
2.3	A more efficient way to compute the summand in equation 2.3	5
3	A convolutional neural network as a choice for f	7
3.1	The convolutional neural network of references [1, 2]	7
3.2	Residual networks: an improved convolutional neural network choice for f	8
3.3	Residual network prediction maps and $G\mu$ posteriors	10
4	Conclusions and a new optimization goal for find f	13
A	Derivation of equation 2.2 from Bayes theorem	15
B	Small gaussian calculation	16

1 Introduction

In recent years there has been a renewed interest in cosmic strings since they can form in a large class of extensions of the Standard Model. Cosmic strings are linear topological defects, remnants of a high-energy phase transition in the very early Universe. The gravitational effects of the string can be parametrized by its string tension $G\mu$, a dimensionless constant where G is Newton's gravitational constant, and μ is the energy per unit length of the string. Because of the continued theoretical uncertainty in cosmic string loop variables, the robust limit on the string tension is provided by long string effects with the best limits coming from the Planck collaboration with $G\mu \lesssim 10^{-7}$ at the 95% confidence level (CL) [3]. See the introductions in [1, 2] for a more detailed discussion and references on these points. As also discussed in that introduction, research for a more sensitive probe of cosmic strings in CMB and 21 cm intensity maps from long string effects have been explored in [4–16]. All of the methods discussed there can be thought of as a statistic on a sky map.

In [1, 2] we proposed a Bayesian interpretation of cosmic string detection where we developed a convolutional neural network to estimate the cosmic string locations in CMB maps, δ_{sky} , and we derived a connection between these estimates and the posterior probability distribution of the cosmic string tension $G\mu$. In this paper we present significant improvements to the calculation of the posterior

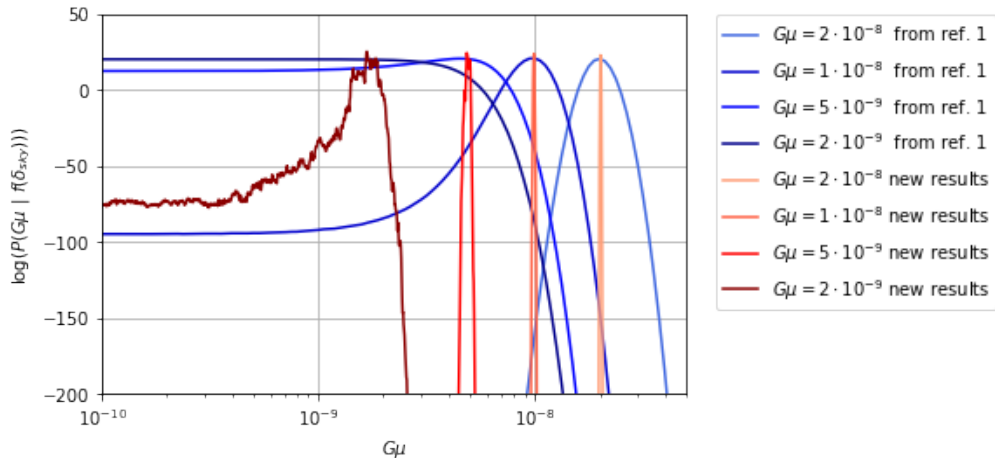


Figure 1: Comparison of the string tension posteriors obtained in reference [1] to the posteriors obtained after the improvements discussed in this paper. These improvements include an improved neural network and the calculation of the posterior using equation 2.13.

distribution of the string tension $G\mu$ and to the convolutional neural network presented in [1, 2]. These improvements are summarized in figure 1 where we plot the logarithm of the posterior probability of the string tension versus string tension. This significant improvement include two effects: an improved neural network and an improvement in our calculation of the posterior probability of the string tension, in particular using equation 2.13.

The improvement in the calculation of the posterior probability is presented in section 2 and it involves two points. The first is a reformulation of the posterior probability in terms of the evidence provided by the neural network evaluated on the sky map, rather than the sky map itself. This allows for a more general and more precise interpretation of our posterior probability formula, as discussed in subsections 2.1 and 2.2. It also allows us to derive a more efficient and accurate way to compute the posterior probability as presented in subsection 2.3. In subsection 3.1 we present the improved posteriors obtained by applying formula 2.13 to the prediction maps using the neural network presented in [1, 2].

The improvement to the plain convolutional neural network involves the use of residual networks [17]. The residual network and the results obtained with it and the new posterior calculation are presented in subsection 3.2 and 3.3. We also compare the prediction maps and posteriors with the results obtained using the old network. We quantify the improvement of the prediction maps by using the standard deviation of the prediction values of the pixel. We quantify the information gained between the old and new posterior distributions by calculating the the Kullback-Leibler (KL) divergence between them.

2 A better way to compute the posterior probability

2.1 The posterior probability in terms of the evidence provided by the neural network

Equation (2.4) of reference [1] expressed the posterior probability of the distribution of the string tension $G\mu$, $P(G\mu | \delta_{sky})$, given the sky map δ_{sky} as evidence. We present it here as equation 2.1:

$$P(G\mu | \delta_{sky}) = \left(\frac{1}{2}\right)^{N_{\text{pixel}}} \left(\frac{P(G\mu)}{P(\delta_{sky})}\right) \left\{ \sum_{\xi \in \Xi} \frac{P(\delta_{sky} | \xi, G\mu) \times P(\xi)}{P(\xi | \delta_{sky}, G\mu)} \right\}. \quad (2.1)$$

ξ is a map which indicates which pixels lie on a string. If $(i, j) \in \text{string}$ then $\xi_{i,j} = 1$, otherwise $\xi_{i,j} = 0$. A map ξ is associated with a CMB temperature map δ_{sky} . We call the space of all such maps Ξ and it contains $2^{N_{\text{pixel}}}$ elements where N_{pixel} is the number of pixels in a map. This formula uses information about the string locations to update our knowledge of the prior distribution $P(G\mu)$ to the posterior $P(G\mu | \delta_{sky})$.

We can be more general, and more precise, by considering $f(\delta_{sky})$ instead of δ_{sky} as evidence, where f can be any function, but we are interested in the case where f is a convolutional neural network. We treat the output of f as evidence and compute the posterior with respect to it: $P(G\mu | f(\delta_{sky}))$. If f is one-to-one, this is the same posterior as $P(G\mu | \delta_{sky})$.

In appendix A we derive the equivalent of equation 2.1 for this case:

$$P(G\mu | f(\delta_{sky})) = \left(\frac{1}{2}\right)^{N_{\text{pixel}}} \frac{P(G\mu)}{P(f(\delta_{sky}))} \frac{1}{N} \sum_{\xi^a \sim P(\xi)} \frac{P(f(\delta_{sky}) | \xi, G\mu)}{P(\xi | f(\delta_{sky}), G\mu)} \quad (2.2)$$

where we have transformed the sum of $\xi \in \Xi$ into an expectation of N maps ξ^a sampled from $P(\xi)$. Thus the factor $P(\xi)$ is not in the summand but in the sampling procedure. Also notice that $2^{N_{\text{pix}}}$, $P(f(\delta_{sky}))$, and N are $G\mu$ independent, hence we can absorb them into the normalisation ($\int P(G\mu | f(\delta_{sky})) dG\mu = 1$). Thus we only need to compute the unnormalized probability $P'(G\mu | f(\delta_{sky}))$:

$$P'(G\mu | f(\delta_{sky})) = P(G\mu) \sum_{\xi^a \sim P(\xi)} \frac{P(f(\delta_{sky}) | \xi^a, G\mu)}{P(\xi^a | f(\delta_{sky}), G\mu)} \quad (2.3)$$

2.2 Conditions on the neural network f

We now make some assumptions regarding the denominator, $P(\xi | f(\delta_{sky}), G\mu)$, and the numerator, $P(f(\delta_{sky}) | \xi, G\mu)$, of the summand of equation 2.3. As in [1], these assumptions encodes our conjecture that we should be able to decide whether a given pixel is on a string without knowing anything about which other pixels are actually on a string. Notice that in this abstraction f is completely free, any function that respects our assumptions below can be used. Most functions

would make the assumptions below quite bad, however, these assumptions are reasonable for the case of the function represented by our neural networks.

1. Conditional independence of each pixel i, j in the answer map ξ and $f(\delta_{sky})$:

$$P(\xi | f(\delta_{sky}), G\mu) = \prod_{i,j} P(\xi_{i,j} | f(\delta_{sky}), G\mu)$$

$$P(f(\delta_{sky}) | \xi, G\mu) = \prod_{i,j} P(f_{i,j}(\delta_{sky}) | \xi, G\mu)$$

2. Each pixel i, j in the answer map depends only on the corresponding pixel in $f(\delta_{sky})$ and vice versa:

$$P(\xi_{i,j} | f(\delta_{sky}), G\mu) = P(\xi_{i,j} | f_{i,j}(\delta_{sky}), G\mu)$$

$$P(f_{i,j}(\delta_{sky}) | \xi, G\mu) = P(f_{i,j}(\delta_{sky}) | \xi_{i,j}, G\mu)$$

3. Translation invariance in the probabilities, i.e. pixel location is not important:

$$\forall i, j, i', j' \text{ where } \xi_{i,j} = \xi_{i',j'} \text{ and } f_{i,j} = f_{i',j'}$$

$$P(\xi_{i,j} | f_{i,j}(\delta_{sky}), G\mu) = P(\xi_{i',j'} | f_{i',j'}(\delta_{sky}), G\mu)$$

and

$$P(f_{i,j}(\delta_{sky}) | \xi_{i,j}, G\mu) = P(f_{i',j'}(\delta_{sky}) | \xi_{i',j'}, G\mu)$$

At this point the only quantities we need to compute are the pixel independent probabilities $P(\xi_{i,j} | f_{i,j}(\delta_{sky}), G\mu)$ and $P(f_{i,j}(\delta_{sky}) | \xi_{i,j}, G\mu)$. These are tractable quantities which we can easily compute from data.

To compute $P(\xi_{i,j} | f_{i,j}(\delta_{sky}), G\mu)$ we begin with a collection of simulated sky maps with strings of a known $G\mu$ and we bin the values that f takes on these maps. For each specific bin, we then take the fraction of pixels which are on strings among the pixels with the specified value of f and assign this value p to $P(\xi_{i,j} = 1 | f_{i,j}(\delta_{sky}))$ and $1 - p$ to $P(\xi_{i,j} = 0 | f_{i,j}(\delta_{sky}))$.

To compute the probability distribution $P(f_{i,j}(\delta_{sky}) | \xi_{i,j}, G\mu)$ we again begin with a collection of simulated sky maps with strings of a known $G\mu$. We then consider all the pixels in our dataset with $\xi_{i,j} = 1$ and compute the histogram of values of f on those pixels. We do the same thing for those pixels with $\xi_{i,j} = 0$.

For the calculations of $P(\xi_{i,j} | f_{i,j}(\delta_{sky}), G\mu)$ and $P(f_{i,j}(\delta_{sky}) | \xi_{i,j}, G\mu)$ that lead to the results we present in section 3 we binned the values of $G\mu$ in 700 bins of equally spaced log intervals between 10^{-11} and 2×10^{-7} :

$$G\mu = 10^{-11+n \times (4+\log_{10} 2)/700}, \quad n = 0, \dots, 700,$$

and the values of f in 1000 equally spaced bins between 0 and 1 with size $1/1000$.

Now that we have the summand it remains to compute the sum over ξ in equation 2.3.

2.3 A more efficient way to compute the summand in equation 2.3

Consider the map ξ^* which maximizes the summand

$$s(\xi^a) \equiv \frac{P(f(\delta_{sky}) | \xi^a, G\mu)}{P(\xi^a | f(\delta_{sky}), G\mu)}. \quad (2.4)$$

$s(\xi^*)$ is then the largest term in the sum of equation 2.3. Note that ξ^* depends on $G\mu$. With the distributional assumptions made in the last section, such a map is easily computable. Because the probability factorises over pixels we can find the maximal map by optimizing each pixel independently. In particular, since

$$s(\xi) = \prod_{i,j} \frac{P(f_{i,j}(\delta_{sky}) | \xi_{i,j}, G\mu)}{P(\xi_{i,j} | f_{i,j}(\delta_{sky}), G\mu)} \equiv \prod_{i,j} s_{i,j}(\xi_{i,j}) \quad (2.5)$$

we have that

$$\xi_{i,j}^* = \begin{cases} 1, & \text{if } s_{i,j}(\xi_{i,j} = 1) > s_{i,j}(\xi_{i,j} = 0) \\ 0, & \text{otherwise} \end{cases} \quad (2.6)$$

Hence computing the maximal map from $f(\delta_{sky})$ is computationally straightforward.

Now consider a map ξ_{-1}^* identical to ξ^* except at 1 pixel, at which the value of ξ_{-1}^* is the opposite of the corresponding value of ξ^* . Since ξ^* is by definition the map which maximizes the probability, the map with 1 pixel reversed will decrease the probability by some value, the new log probability is

$$\begin{aligned} \log s(\xi_{-1}^*) &= \sum_{i,j} \log(s_{i,j}(\xi_{-1,i,j}^*)) \\ &= \log(s_{i',j'}(1 - \xi_{i',j'}^*)) + \sum_{i,j \neq i',j'} \log(s_{i,j}(\xi_{i,j}^*)) \\ &= \log(s_{i',j'}(1 - \xi_{i',j'}^*)) - \log(s_{i',j'}(\xi_{i',j'}^*)) + \log(s(\xi^*)) \end{aligned} \quad (2.7)$$

where (i', j') is the pixel by which ξ^* and ξ_{-1}^* differ.

We can compute the expected change over all maps with a single misplaced pixel by simply averaging over pixels:

$$\begin{aligned} \Delta_{-1}^*(f, G\mu) &\equiv \left\langle \log s(\xi_{-1}^*) - \log s(\xi^*) \right\rangle \\ &= \frac{1}{N_{pix}} \sum_{i,j} \left(\log(s_{i,j}(1 - \xi_{i,j}^*)) - \log(s_{i,j}(\xi_{i,j}^*)) \right) \end{aligned} \quad (2.8)$$

To recapitulate, $\Delta_{-1}(f, G\mu)$ is defined as the expected change in the log conditional probability of the evidence $f(\delta_{sky})$ as we condition on ξ maps with only 1 pixel difference from the maximal map. Similarly, we define $\Delta_{-n}(f, G\mu)$ as the equivalent expectation taken over maps which differ by n pixels from the maximal map. By independence of pixels we have (to a very good approximation when n is low compared to the map size) that

$$\Delta_{-n}^*(f, G\mu) = n \times \Delta_{-1}^*(f, G\mu)$$

i.e. the expected change in the log probability incurred by changing n pixels from the maximal map is simply n times that of the expectation of changing 1 pixel. This is not strictly correct, there are some errors involved from double counting the pixels, however, at low n (where the probabilities are largest and most important) these errors are insignificant. If this error seems to become significant at high enough n , we cannot use the analytic method anymore and must resort to computing $\Delta_{-n}^*(f, G\mu)$ by drawing samples of n pixels and observing the empirical expected change in log probability over multiple samples.

Using the equations above we can finally approximate $\log s(\xi)$ as

$$\log s(\xi) \approx \log s(\xi^*) + n_{\xi^*, \xi} \times \Delta_{-1}^*(f, G\mu) \quad (2.9)$$

where $n_{\xi^*, \xi}$ is the number of differences between ξ^* and ξ .

We use the results above to significantly simplify the posterior probability calculation currently given in terms of a sum over Boolean maps in equation 2.3. Starting with equation 2.3 and using equation 2.9 we have

$$\begin{aligned} P'(G\mu | f(\delta_{sky})) &= P(G\mu) \sum_{\xi} \frac{P(f(\delta_{sky}) | \xi, G\mu)}{P(\xi | f(\delta_{sky}), G\mu)} \times P(\xi) \\ &= P(G\mu) \sum_{\xi} \exp\left(\log s(\xi)\right) \times P(\xi) \\ &\approx P(G\mu) \sum_{\xi} \exp\left(\log s(\xi^*) + n_{\xi^*, \xi} \times \Delta_{-1}^*(f, G\mu)\right) \times P(\xi) \\ &= P(G\mu) s(\xi^*) \sum_{\xi} \exp\left(n_{\xi^*, \xi} \times \Delta_{-1}^*(f, G\mu)\right) \times P(\xi) \quad (2.10) \end{aligned}$$

Notice that inside the sum over all Boolean maps ξ , maps contribute to the sum only through $n_{\xi^*, \xi}$. Two maps for which this factor is identical will contribute the same amount to the sum (relative to their prior probabilities), hence we can write:

$$\begin{aligned} \sum_{\xi} \exp\left(n_{\xi^*, \xi} \times \Delta_{-1}^*(f, G\mu)\right) \times P(\xi) &= \\ \sum_n \exp\left(n \times \Delta_{-1}^*(f, G\mu)\right) \times \sum_{n_{\xi^*, \xi}=n} P(\xi) &\quad (2.11) \end{aligned}$$

All that remains to be done now is to compute the remaining sums over ξ at the end of the last equation, we have:

$$\sum_{n_{\xi^*, \xi}=n} P(\xi) = P(n|\xi^*)$$

i.e. the probability of a map ξ having n pixels different from ξ^* . We would like to calculate the probability $P(n|\xi^*)$ using histograms. That is, we have the maps

ξ^* as well as a dataset of maps ξ^a sampled from $P(\xi)$, so we would like to simply directly evaluate n_{ξ^*, ξ^a} and plot its histogram to get the probability distribution. However, the 450 map dataset we used does not contain any maps at small n , so we will not have any bins for those n where the terms in the sum are largest. For this reason we extrapolate the behaviour at low n based on the behaviour at the n we do encounter and we approximate $P(n|\xi^*)$ as a gaussian and compute the mean and standard deviation from data we do have. For the maps we use (see section 3) the number of pixels is $N_{pix} = 512 \times 512 \approx 2.6 \times 10^5$, and the mean and standard deviation of $P(n|\xi^*)$ are of order 10^5 and 7000, respectively.

To recap, we have transformed a sum with $2^{N_{pix}}$ terms (the sum over the Boolean maps with N_{pix} pixels) into a sum over the integer n between 0 and N_{pix} . Needless to say, the latter is significantly more tractable than the former. Putting everything back together, we obtain that the posterior probability of $G\mu$ conditioned on the evidence produced by a function f is

$$P'(G\mu | f(\delta_{sky})) \approx P(G\mu) \frac{P(f(\delta_{sky}) | \xi^*, G\mu)}{P(\xi^* | f(\delta_{sky}), G\mu)} \times \sum_{n=0}^{N_{pix}} \exp\left(n \times \Delta_{-1}^*(f, G\mu)\right) \times P(n|\xi^*) \quad (2.12)$$

Using the gaussian calculation we present in appendix B, this can be rewritten in terms of the mean μ and standard deviation σ of $P(n|\xi^*)$ as

$$P'(G\mu | f(\delta_{sky})) \approx P(G\mu) \frac{P(f(\delta_{sky}) | \xi^*, G\mu)}{P(\xi^* | f(\delta_{sky}), G\mu)} \times \exp\left(\mu\Delta_{-1}^* + \sigma^2(\Delta_{-1}^*)^2/2\right) \times \frac{1}{2} \left(\text{Erfc}\left(\frac{N_{pix} - (\mu + \sigma^2\Delta_{-1}^*)}{\sqrt{2}\sigma^2}\right) - \text{Erfc}\left(-\frac{\mu + \sigma^2\Delta_{-1}^*}{\sqrt{2}\sigma^2}\right) \right) \quad (2.13)$$

This is the formula we will use from now on to calculate the Bayesian posterior distribution of the string tension.

3 A convolutional neural network as a choice for f

3.1 The convolutional neural network of references [1, 2]

One choice for the function f is the 5 layer convolutional neural network described in detail in [2]. The first layer involved a convolution map on the scalar valued pixels and gives a 32 dimensional value for each pixel. Each subsequent layer of the network involves a convolution map on N_{pix} elements with the fol-

lowing structure (the terms "kernel size" and "stride" are defined in [2]):

$$\begin{aligned}
&\text{layer 1 : 1-dim} \rightarrow \text{32-dim, kernel size} = 3, \text{stride} = 1 \\
&\qquad\qquad\qquad\downarrow \text{tanh} \\
&\text{layer 2 : 32-dim} \rightarrow \text{32-dim, kernel size} = 3, \text{stride} = 1 \\
&\qquad\qquad\qquad\downarrow \text{tanh} \\
&\text{layer 3 : 32-dim} \rightarrow \text{32-dim, kernel size} = 3, \text{stride} = 1 \\
&\qquad\qquad\qquad\downarrow \text{tanh} \\
&\text{layer 4 : 32-dim} \rightarrow \text{32-dim, kernel size} = 3, \text{stride} = 1 \\
&\qquad\qquad\qquad\downarrow \text{tanh} \\
&\text{layer 5 : 32-dim} \rightarrow \text{1-dim, kernel size} = 1, \text{stride} = 1 \qquad (3.1)
\end{aligned}$$

From this we see that the network has 28 097 parameters:

$$\{(32 \cdot 3^2 + 32) + (32^2 \cdot 3^2 + 32) \times 3 + 32 + 1\} = 28\,097 .$$

We trained this network by minimizing the cross entropy given by the Kullback-Leibler divergence between the probability $P(\xi | \delta_{sky}, G\mu)$ and the parametrised convolutional neural network that we used to approximate that probability (equation (4.7) in [1] or equation (2.2) in [2]).

To obtain the posterior probability for the string tension in reference [1], we considered equations (2.4) or (4.8). Without the technique described in section 2.3 above, this is a computationally difficult task so instead we approximated the posterior probability in the following way. We used the neural network f to evaluate the sky map δ_{sky} with the unknown string tension and we binned the values $f_{i,j}(\delta_{sky})$ of each pixel into 1000 bins between 0 and 1. We then calculated the χ^2 of the histogram $f(\delta_{sky})$ to a data set of histograms of $f_{i,j}$ values obtained from maps with known $G\mu$. This gave us an estimate of the string tension's posterior probability. In figure 2 we compare this posterior probability from reference [1] to that obtained by calculating with equation 2.13. We see that the posterior estimates presented in [1] were conservative and that the direct calculation of the Bayesian posterior probability of $G\mu$ gives much sharper peaks.

3.2 Residual networks: an improved convolutional neural network choice for f

Simply adding more layers to the neural network in [1] gave us a network that we were unable to train. By that we mean that the cross entropy did not decrease and converge to a lower value after each training iteration. One technique used to train deeper neural networks is to use a residual network [17]. We experimented with residual networks between 5 and 100 layers and were able to have training converge for all of them. However we found that the results from using more than 30 layer network were not significantly better. In this section we describe our residual network and then present and compare the results of the 30 layer residual network to those of our previous work [1, 2].

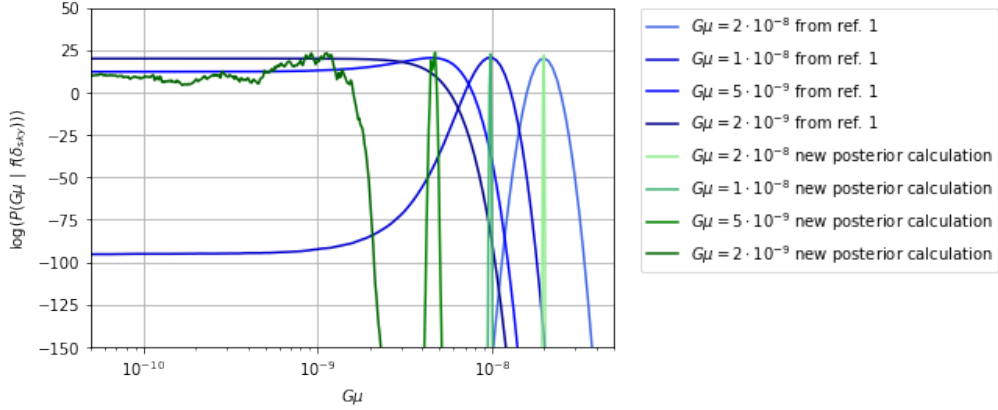


Figure 2: Comparison of the posteriors obtained in reference [1] and the posteriors calculated for the same network using equation 2.13.

Whereas plain convolutional neural networks can only propagate forward to the next layer, residual networks allow for additional shortcut propagation from one layer to another one a few layers away. These few layers that can be skipped over form what is called a residual block. Our 30 layer residual network consisted of 30 residual blocks sandwiched between an initial and a final layer. Each block contained 3 layers. Our residual network had the following structure for the convolution of each pixel:

initial layer : 1-dim \rightarrow 32-dim, kernel size = 3, stride = 1

\downarrow

residual block 1: 32-dim \rightarrow 32-dim

\downarrow

residual block 2: 32-dim \rightarrow 32-dim

\downarrow

...

\downarrow

residual block 30: 32-dim \rightarrow 32-dim

\downarrow

final layer 5 : 32-dim \rightarrow 1-dim, kernel size = 1, stride = 1

In addition to being able to go through the block, one can go around the block and begin at the next block down. Each of the 30 residual blocks is composed

of the following 3 layers:

$$\begin{aligned}
&\text{layer 1 : } 32\text{-dim} \rightarrow 8\text{-dim, kernel size} = 1, \text{stride} = 1 \\
&\quad \downarrow \text{tanh} \\
&\text{layer 2 : } 8\text{-dim} \rightarrow 8\text{-dim, kernel size} = 3, \text{stride} = 1 \\
&\quad \downarrow \text{tanh} \\
&\text{layer 3 : } 8\text{-dim} \rightarrow 32\text{-dim, kernel size} = 1, \text{stride} = 1
\end{aligned}$$

The number of parameters in our residual network is 65 857.

$$\{(32+32)+(32^2+32)\times 30+(32\cdot 8+8+8^2\cdot 3^2+8+8\cdot 32+32)\times 30+32+1\} = 65\,857.$$

We trained the residual network in the same way we trained our previous network [1]. We used numerically generated CMB temperature maps with and without cosmic strings. The dataset was obtained with the same long string analytical model [18] used in [1] and other previous studies of cosmic string detection in CMB maps [10–13]. We used the PyTorch environment (pytorch.org) for machine learning and optimization algorithms, and we trained the model on a Tesla K80 GPU for 12 hours in total.

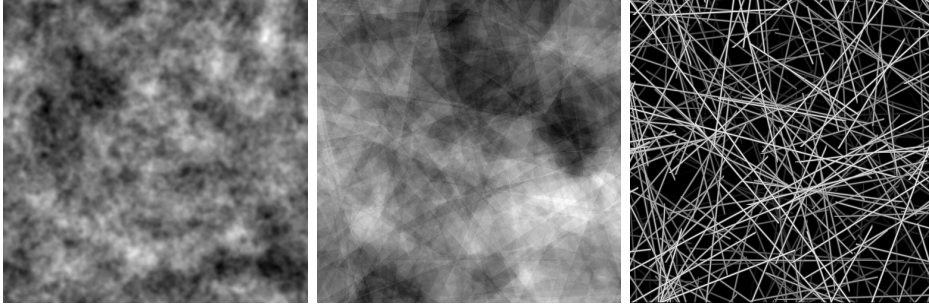
The maps were made up of 512×512 pixels with a resolution of 1 arcminute per pixel. This leads to the sky map show in Fig. 3a. For values of the string tension we study here, $G\mu \leq 2 \times 10^{-8}$, the sky map is indistinguishable by eye from a pure Gaussian fluctuation map (i.e. $G\mu = 0$). The string temperature component to the full sky map is shown in Fig. 3b with a $G\mu = 1$. One of the unknown parameters characterizing the scaling solution of strings is the number of strings per Hubble volume, N_H , which can have a value between 1 and 10. We trained our neural network with a value of $N_H = 1$ and this did not impair the predictive power for input maps with larger N_H values. This is an indication that the network is indeed generalizing and not just overfitting.

3.3 Residual network prediction maps and $G\mu$ posteriors

In Fig. 4 we show our residual and plain network predictions for the string location map using different values for $G\mu$, with $N_H = 3$, and no noise. The shades of grey in the prediction maps correspond to the probability of a pixel being on a string. Completely black pixels are probability 0 and completely white pixels are probability 1 of being on a string. As $G\mu$ tends to zero, the neural network provides less information as to whether a pixel is on a string or not and the pixel probabilities tend to the prior $P((i, j) \in \text{string})$ which is given by the number of pixels on strings in the answer map ξ (fig. 3c) divided by the total number of pixels. Thus as $G\mu$ tends to zero, our prediction map will become more uniformly grey, as figures 4e,4f show.

The two predictions maps look different, though it is not immediately clear that the residual network is better. However with a careful visual comparison of the prediction maps from the two networks we see that the residual network is

Figure 3: CMB anisotropy temperature maps of 512×512 pixels with a resolution of 1 arcminute per pixel. The white and black pixels are $+450\mu\text{K}$ and $-450\mu\text{K}$ anisotropies, respectively. The shades of grey of the strings in the string answer map correspond to the relative strength of the string’s GKS temperature discontinuity.



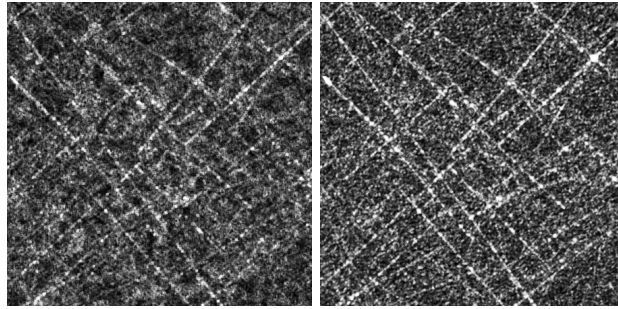
(a) The full sky map, δ_{sky} . (b) String component contribution δ_{string} to the full sky map. (c) String answer map ξ used in the simulation. Maps with and without strings are indistinguishable by eye.

distinguishing the string locations more clearly. In fact we show in figure 5 that the prediction values in the residual network have a standard deviation that is larger than our old network. The mean value of the predictions is the same, yet the residual network assigns more high and low probability values than our old network. In other words, the residual network’s certainty of which pixels contain strings, and which pixels do not, is greater than for that of the old network.

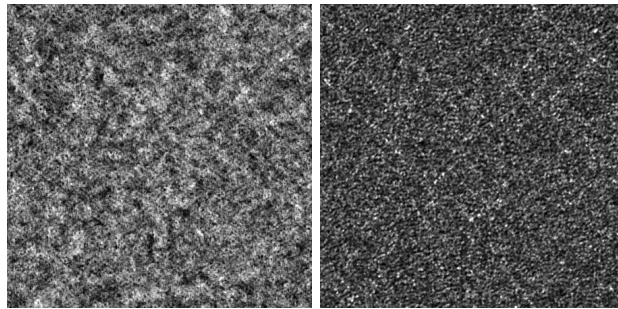
However the real test of the superior performance of the residual network is the posterior probability of the string tension that it provides through equation 2.13. In figure 6 we compare the posteriors obtained from the old neural network to those obtained from the residual network, both calculated with equation 2.13. The improvement shown in figure 6 plus the improvement presented in figure 2 results in the total improvement we presented in figure 1 of the introduction.

From figure 6 we see that all the peaks in the posterior distribution from the residual network are sharper and more accurately centred over the true value of $G\mu$. For $G\mu = 2 \times 10^{-9}$ the residual network provides a clear bump over the correct string tension, whereas the old network does not. Calculating the area under the probability given by this bump tells us that there is a 0.99 probability that $G\mu \in [1.7, 2.1] \times 10^{-9}$.

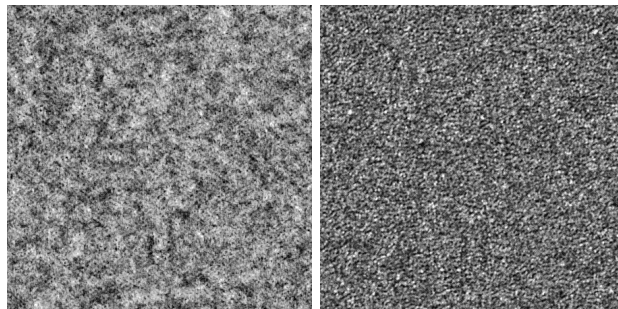
Our posteriors contain information and allow us to provide *lower* limits on the string tension, even when they do not produce a bump in $G\mu$. For example, consider the sky map with strings of $G\mu = 1 \times 10^{-9}$ and its posterior as shown in figure 6. That posterior predicts a 0.99 probability that $G\mu > 2 \times 10^{-11}$. The same analysis on a sky map with $G\mu = 1.6 \times 10^{-9}$ gives $G\mu > 1.3 \times 10^{-9}$.



(a) Reference [1] prediction $G\mu = 10^{-8}$ (b) Residual network prediction $G\mu = 10^{-8}$



(c) Reference [1] prediction $G\mu = 5 \times 10^{-9}$ (d) Residual network prediction $G\mu = 5 \times 10^{-9}$



(e) Reference [1] prediction $G\mu = 2 \times 10^{-9}$ (f) Residual network prediction $G\mu = 2 \times 10^{-9}$

Figure 4: Comparison of Neural Network Predictions Without Noise.

The actual placement of long strings, the ξ map, is given in 3c. We compare our neural network’s prediction of ξ for different value of the string tension with no noise for the network used in [1] on the left, and the residual network introduced here on the right. The shades of grey in the prediction maps correspond to the probability of a pixel being on a string, with completely black pixels being 0 probability and completely white pixels being probability 1. All the figures correspond to 512×512 pixels with a resolution of 1 arcminute per pixel.

The Kullback-Leibler divergence allows us to quantify how much more information is gained in going from the posterior probabilities of our old network P_{old} ,

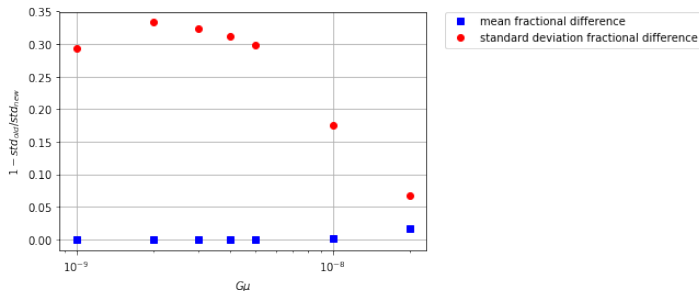


Figure 5: Comparison of mean and standard deviation over pixels in the prediction maps of the two networks. We plot the fractional difference between the two networks, $1 - \frac{\text{old network}}{\text{residual network}}$.

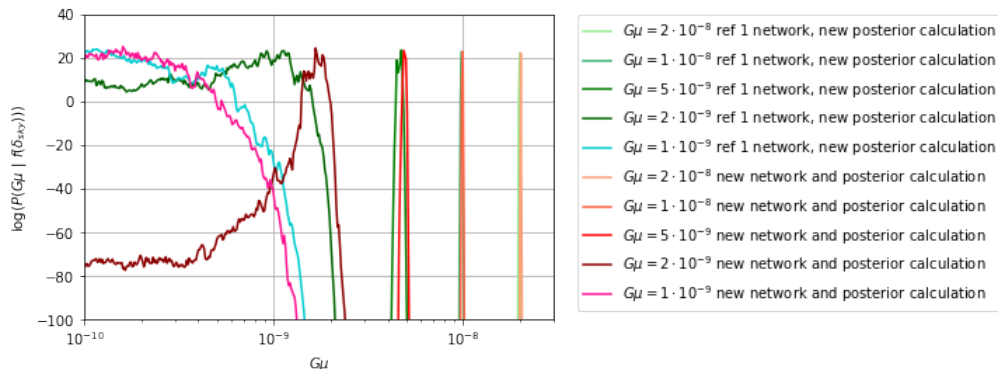


Figure 6: Comparison of the posteriors improvement obtained by using the residual network in place of the network from reference [1]. In both cases the posteriors are calculated using equation 2.13.

to that of the residual network P_{new} :

$$D_{KL}(P_{old}||P_{new}) \equiv \int d(G\mu) P_{old}(G\mu) \log \frac{P_{old}(G\mu)}{P_{new}(G\mu)} \quad (3.2)$$

In figure 7 we plot the value of the KL divergence at various string tensions between the two posteriors given in figures 1,2,6.

4 Conclusions and a new optimization goal for find f

In our previous work [1, 2] we presented a Bayesian interpretation of cosmic string detection in which the posterior probability distribution of the string tension is linked to the estimates of cosmic string location on a CMB map. Here we have presented a reformulation of the posterior formula and introduced a more efficient and accurate way to compute the posterior probability. In addition we have improved our convolutional neural network with residual networks to yield better prediction maps and posterior probabilities for the string tension. We have

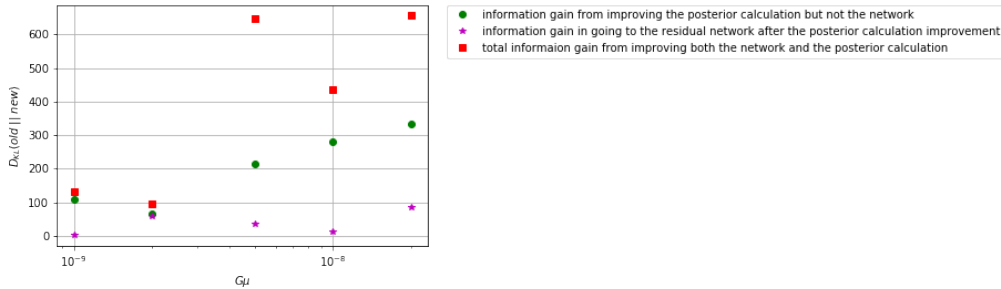


Figure 7: Information gain on the posterior distribution of the string tension from analyzing sky maps with the residual network and the new calculation of the posterior using equation 2.13, versus network and the calculation from reference [1]

presented and quantified these improvements in subsection 3.2 and 3.3. All these improvements together can be summarized by figure 1 in the introduction.

We have improved our previous neural network by using the more sophisticated architecture provided by residual networks [17] as a preamble to introducing noise and then applying our analysis to realistic string simulations ([3, 19], work in progress). While we have presented our analysis in the context of cosmic string detection in CMB temperature anisotropy maps, generalizing the procedure to cosmic string wake detection in 21 cm intensity maps is straightforward [4–8].

Our derivation of a posterior probability for the string tension was specifically done in order to derive a connection between the string tension and the location of cosmic strings on a map. We then trained our neural network f to be good at estimating string locations. We did this by minimizing the KL divergence between $f(\delta_{sky})$ and $P(\xi|\delta_{sky})$. Thus ”good” functions f are those that produce outputs that resemble the true answer map ξ . The network has no knowledge of our Bayesian formula connecting these string locations to the string tension. And while we can experimentally verify that the function which optimizes the KL divergence leads to good posteriors, it is unlikely to be the best one. All this suggests that another way of obtaining f would be to directly optimize the posterior probability distributions. Since the derivations of section 2 were all made in a way agnostic to f , any function $f : R^{N_{pix}} \rightarrow R^{N_{pix}}$ can be plugged-in the calculations and the procedure will spit out the corresponding posteriors. Hence the bayesian procedure derived in the previous sections implicitly provides a criterion to evaluate the ”goodness” of various functions f : on average, does f lead to sharp posteriors centred around the correct $G\mu$? It would be interesting to see if we still obtain ”good” prediction maps when f is chosen in this way.

Acknowledgments

We thank Christophe Ringeval for useful discussions. We acknowledge the support of the Fonds de recherche du Québec – Nature et technologies (FRQNT) Programme de recherche pour les enseignants de collège, and the support of the Natural Sciences and Engineering Research Council of Canada (NSERC) [funding reference number SAPIN-2018-00020]. Computations were made on the supercomputer Helios from Université Laval, managed by Calcul Québec and Compute Canada. The operation of this supercomputer is funded by the Canada Foundation for Innovation (CFI), the ministère de l'Économie, de la science et de l'innovation du Québec (MESI) and the Fonds de recherche du Québec – Nature et technologies (FRQNT).

Appendices

A Derivation of equation 2.2 from Bayes theorem

Consider:

$$P(\xi | f(\delta_{sky}), G\mu) = \frac{P(f(\delta_{sky}), G\mu | \xi)P(\xi)}{P(f(\delta_{sky}), G\mu)}$$

$$P(\xi | f(\delta_{sky}), G\mu) = \frac{P(f(\delta_{sky}), G\mu | \xi)P(\xi)}{P(G\mu | f(\delta_{sky}))P(f(\delta_{sky}))}$$

shuffling terms around and using $P(f(\delta_{sky}), G\mu | \xi) = P(f(\delta_{sky}) | \xi, G\mu)P(G\mu | \xi) = P(f(\delta_{sky}) | \xi, G\mu)P(G\mu)$:

$$P(G\mu | f(\delta_{sky})) = \frac{P(f(\delta_{sky}) | \xi, G\mu) \times P(G\mu) \times P(\xi)}{P(\xi | f(\delta_{sky}), G\mu) \times P(f(\delta_{sky}))}$$

Summing over all Boolean maps ξ :

$$2^{N_{pix}} P(G\mu | f(\delta_{sky})) = \sum_{\xi} \frac{P(f(\delta_{sky}) | \xi, G\mu) \times P(G\mu) \times P(\xi)}{P(\xi | f(\delta_{sky}), G\mu) \times P(f(\delta_{sky}))}$$

$$2^{N_{pix}} P(G\mu | f(\delta_{sky})) = \frac{P(G\mu)}{P(f(\delta_{sky}))} \sum_{\xi} \frac{P(f(\delta_{sky}) | \xi, G\mu) \times P(\xi)}{P(\xi | f(\delta_{sky}), G\mu)}$$

Transforming the sum into an expectation over maps ξ^a sampled from $P(\xi)$ and switching the factor of $2^{N_{pix}}$ to the right:

$$P(G\mu | f(\delta_{sky})) = 2^{-N_{pix}} \frac{P(G\mu)}{P(f(\delta_{sky}))} \frac{1}{N} \sum_{\xi^a \sim P(\xi)} \frac{P(f(\delta_{sky}) | \xi^a, G\mu)}{P(\xi^a | f(\delta_{sky}), G\mu)}$$

B Small gaussian calculation

We present the calculation used to go from equation 2.12 to 2.13.

$$\begin{aligned}
& \sum_{n=0}^N \exp(n \times \Delta_{-1}^*) \frac{1}{\sqrt{2\pi\sigma^2}} \exp\left(-\frac{(n-\mu)^2}{2\sigma^2}\right) \\
&= \sum_{n=0}^N \frac{1}{\sqrt{2\pi\sigma^2}} \exp\left(n\Delta_{-1}^* - \frac{(n-\mu)^2}{2\sigma^2}\right) \\
&= \sum_{n=0}^N \frac{1}{\sqrt{2\pi\sigma^2}} \exp\left(-\frac{(n-\mu)^2 - 2\sigma^2 n\Delta_{-1}^*}{2\sigma^2}\right) \\
&= \sum_{n=0}^N \frac{1}{\sqrt{2\pi\sigma^2}} \exp\left(-\frac{n^2 - 2n\mu + \mu^2 - 2\sigma^2 n\Delta_{-1}^*}{2\sigma^2}\right) \\
&= \sum_{n=0}^N \frac{1}{\sqrt{2\pi\sigma^2}} \exp\left(-\frac{(n - (\mu + \sigma^2\Delta_{-1}^*))^2 + \mu^2 - (\mu + \sigma^2\Delta_{-1}^*)^2}{2\sigma^2}\right) \\
&= \exp\left(-\frac{\mu^2 - (\mu + \sigma^2\Delta_{-1}^*)^2}{2\sigma^2}\right) \times \int_0^N \frac{1}{\sqrt{2\pi\sigma^2}} \exp\left(-\frac{(n - (\mu + \sigma^2\Delta_{-1}^*))^2}{2\sigma^2}\right) \\
&= \exp\left(-\frac{-2\mu\sigma^2\Delta_{-1}^* - (\sigma^2\Delta_{-1}^*)^2}{2\sigma^2}\right) \times \frac{1}{2} \left(-\text{Erf}\left(\frac{(\mu + \sigma^2\Delta_{-1}^*) - N}{\sqrt{2\sigma^2}}\right) + \text{Erf}\left(\frac{\mu + \sigma^2\Delta_{-1}^*}{\sqrt{2\sigma^2}}\right)\right) \\
&= \exp(\mu\Delta_{-1}^* + \sigma^2(\Delta_{-1}^*)^2/2) \times \frac{1}{2} \left(-\text{Erf}\left(\frac{(\mu + \sigma^2\Delta_{-1}^*) - N}{\sqrt{2\sigma^2}}\right) + \text{Erf}\left(\frac{\mu + \sigma^2\Delta_{-1}^*}{\sqrt{2\sigma^2}}\right)\right) \\
&= \exp(\mu\Delta_{-1}^* + \sigma^2(\Delta_{-1}^*)^2/2) \times \frac{1}{2} \left(\text{Erfc}\left(\frac{N - (\mu + \sigma^2\Delta_{-1}^*)}{\sqrt{2\sigma^2}}\right) - \text{Erfc}\left(-\frac{\mu + \sigma^2\Delta_{-1}^*}{\sqrt{2\sigma^2}}\right)\right)
\end{aligned}$$

References

- [1] Razvan Ciuca and Oscar F Hernández. A Bayesian framework for cosmic string searches in CMB maps. *Journal of Cosmology and Astroparticle Physics*, 2017(08):028–028, August 2017. doi:10.1088/1475-7516/2017/08/028. URL <http://iopscience.iop.org/article/10.1088/1475-7516/2017/08/028>.
- [2] Razvan Ciuca, Oscar F Hernández, and Michael Wolman. A Convolutional Neural Network For Cosmic String Detection in CMB Temperature Maps. August 2017. URL <https://arxiv.org/abs/1708.08878>. 1708.08878.
- [3] Planck Collaboration, P A R Ade, N Aghanim, et al. Planck 2013 results. XXV. Searches for cosmic strings and other topological defects. *Astronomy and Astrophysics*, 571:A25–21, October 2014. doi:10.1051/0004-6361/201321621. URL <http://www.aanda.org/10.1051/0004-6361/201321621>.
- [4] Robert H Brandenberger, Rebecca J Danos, Oscar F Hernández, and Gilbert P Holder. The 21 cm signature of cosmic string wakes. *Journal of Cosmology and Astroparticle Physics*, 2010(12):028–028, December 2010. doi:10.1088/1475-7516/2010/12/028. URL <http://stacks.iop.org/1475-7516/2010/i=12/a=028?key=crossref.06cd636240d3dcc2a318c128fbf19911>.
- [5] Oscar F Hernández, Yi Wang, José Fong, and Robert H Brandenberger. Angular 21 cm power spectrum of a scaling distribution of cosmic string wakes. *Journal of Cosmology and Astroparticle Physics*, 2011(08):014–014, August 2011. doi:10.1088/1475-7516/2011/08/014. URL <http://stacks.iop.org/1475-7516/2011/i=08/a=014?key=crossref.978931ecf93cfc12630b475edc7289d3>.
- [6] Oscar F Hernández and Robert H Brandenberger. The 21 cm signature of shock heated and diffuse cosmic string wakes. *Journal of Cosmology and Astroparticle Physics*, 2012(07):032–032, July 2012. doi:10.1088/1475-7516/2012/07/032. URL <http://stacks.iop.org/1475-7516/2012/i=07/a=032?key=crossref.b3a19d57f7e6bacc07732ecc03c756c6>.
- [7] Oscar F Hernández. Wouthuysen-Field absorption trough in cosmic string wakes. *Physical Review D*, 90(12):123504–9, December 2014. doi:10.1103/PhysRevD.90.123504. URL <http://link.aps.org/doi/10.1103/PhysRevD.90.123504>.
- [8] Disrael Camargo Neves da Cunha, Robert H Brandenberger, and Oscar F Hernández. Disruption of cosmic string wakes by Gaussian fluctuations. *Physical Review D*, 93(12):123501–8, June 2016. doi:10.1103/PhysRevD.93.123501. URL <http://link.aps.org/doi/10.1103/PhysRevD.93.123501>.
- [9] Aaron Berndsén, Levon Pogossian, and Mark Wyman. Correlations between 21-cm radiation and the cosmic microwave background from active sources. *Monthly Notices of the Royal Astronomical Society*, 407(2):1116–1122, July 2010. doi:10.1111/j.1365-2966.2010.16951.x. URL <http://mnras.oxfordjournals.org/cgi/doi/10.1111/j.1365-2966.2010.16951.x>.
- [10] Stephen Amsel, Joshua Berger, and Robert H Brandenberger. Detecting cosmic strings in the CMB with the Canny algorithm. *Journal of Cosmology and Astroparticle Physics*, 2008(04):015–14, April 2008. doi:10.1088/1475-7516/2008/04/015. URL <http://stacks.iop.org/1475-7516/2008/i=04/a=015?key=crossref.169813d11e11398049cbaf828d9a491b>.
- [11] Andrew Stewart and Robert H Brandenberger. Edge detection, cosmic strings and the south pole telescope. *Journal of Cosmology and Astroparticle Physics*,

- 2009(02):009–009, February 2009. doi:10.1088/1475-7516/2009/02/009. URL <http://stacks.iop.org/1475-7516/2009/i=02/a=009?key=crossref.bc207dc093ea8dd54c4b90518d76a15d>.
- [12] Rebecca J Danos and Robert H Brandenberger. Canny Algorithm, Cosmic Strings and the Cosmic Microwave Background. *International Journal of Modern Physics D*, 19(0):183–217, 2010. doi:10.1142/S0218271810016324. URL http://adsabs.harvard.edu/cgi-bin/nph-data_query?bibcode=2010IJMPD..19..183D&link_type=EJOURNAL.
- [13] Lukas Hergt, Adam Amara, Robert H Brandenberger, Tomasz Kacprzak, and Alexandre Refregier. Searching for cosmic strings in CMB anisotropy maps using wavelets and curvelets. *Journal of Cosmology and Astroparticle Physics*, 2017(06):004–004, June 2017. doi:10.1088/1475-7516/2017/06/004. URL <http://iopscience.iop.org/article/10.1088/1475-7516/2017/06/004>.
- [14] J D McEwen, S M Feeney, H V Peiris, et al. Wavelet-Bayesian inference of cosmic strings embedded in the cosmic microwave background. *Monthly Notices of the Royal Astronomical Society*, 472(4):4081–4098, December 2017. doi:10.1093/mnras/stx2268. URL <http://academic.oup.com/mnras/article/472/4/4081/4104647/WaveletBayesian-inference-of-cosmic-strings>.
- [15] A Vafaei Sadr, S M S Movahed, M Farhang, et al. A Multiscale pipeline for the search of string-induced CMB anisotropies. *Monthly Notices of the Royal Astronomical Society*, 475(1):1010–1022, March 2018. doi:10.1093/mnras/stx3126. URL <http://academic.oup.com/mnras/article/475/1/1010/4743743>.
- [16] A Vafaei Sadr, M Farhang, S M S Movahed, B Bassett, and M Kunz. Cosmic string detection with tree-based machine learning. *Monthly Notices of the Royal Astronomical Society*, 478(1):1132–1140, July 2018. doi:10.1093/mnras/sty1055. URL <https://academic.oup.com/mnras/article/478/1/1132/4990649>.
- [17] Kaiming He, Xiangyu Zhang, Shaoqing Ren, and Jian Sun. Deep Residual Learning for Image Recognition. December 2015. URL <https://arxiv.org/abs/1512.03385>. 1512.03385.
- [18] Leandros Perivolaropoulos. COBE versus cosmic strings. An analytical model. *Physics Letters B*, 298(3-4):305–311, January 1993. doi:10.1016/0370-2693(93)91825-8. URL <http://linkinghub.elsevier.com/retrieve/pii/0370269393918258>.
- [19] Aurelien A Fraisse, Christophe Ringeval, David N Spergel, and François R Bouchet. Small-Angle CMB Temperature Anisotropies Induced by Cosmic Strings. D78(4):043535, 2008. doi:10.1103/PhysRevD.78.043535. URL <https://link.aps.org/doi/10.1103/PhysRevD.78.043535>.